A discrete dislocation analysis of residual stresses in a composite material

Cleveringa, H.H.M.; van der Giessen, E.; Needleman, A.

Published in:
Philosophical Magazine A-Physics of Condensed Matter Structure Defects and Mechanical Properties

DOI:
10.1080/01418619908210338

Publication date:
1999

PHILOSOPHICAL MAGAZINE A, 1999, VOL. 79, NO. 4, 893–920

A discrete dislocation analysis of residual stresses in a composite material

H. H. M. CLEVERINGA, E. VAN DER GIESSEN

Delft University of Technology, Koiter Institute Delft, Mekelweg 2, 2628 CD Delft, The Netherlands

and A. NEEDLEMAN

Brown University, Division of Engineering, Providence, Rhode Island 02912, USA

[*Received 9 January 1998 and accepted in revised form 15 June 1998*]

ABSTRACT

Residual stresses and strains in a two-dimensional model composite consisting of elastic reinforcements in a crystalline matrix are analysed. The composite is subject to macroscopic shear and then unloaded. Plane-strain conditions and single slip on slip planes parallel to the shear direction are assumed. The dislocations are modelled as line defects in a linear elastic medium. At each stage of loading, superposition is used to represent the solution in terms of the infinite medium solution for the discrete dislocations and an image solution that enforces the boundary conditions, which is non-singular and obtained from a linear elastic finite-element solution. The lattice resistance to dislocation motion, dislocation nucleation and dislocation annihilation are incorporated into the formulation through a set of constitutive rules. Obstacles leading to possible dislocation pile-ups are also accounted for. Considerable reverse plasticity is found when the reinforcement arrangement is such that all slip planes are cut by particles and when the unloading rate is equal to the loading rate. When unloading takes place at a very high rate, the unloading slope is essentially elastic but relaxation of the dislocation structure occurs in the unloaded state. Predictions of the discrete dislocation formulation for residual stresses, residual strains and the strain variance are compared with corresponding predictions obtained using conventional continuum slip crystal plasticity. The effect of particle size, as predicted by the discrete dislocation description, is also addressed.

§1. INTRODUCTION

Residual stresses are inherent in composites owing to the mismatch in properties between the reinforcement and the matrix. Differences in thermal expansion induce residual stresses during processing. Under mechanical loading, the presence of the reinforcement in metal-matrix composites promotes inhomogeneous plastic flow in the matrix, resulting in residual stresses when the applied loads are removed. However generated, residual stresses affect the subsequent mechanical behaviour, leading, for example, to an inequality between the tensile and compressive yield strengths (Arsenault and Taya 1987, Warner and Stobbs 1989, Taggert and Bassani 1991, Zahl and McMeeking 1991).

Several approaches have been used to predict residual stresses in metal-matrix composites including mean-field theories (for example Arsenault and Taya (1987),

Withers *et al.* (1989) and Clyne and Withers (1993)) and full field numerical solutions for idealized periodic reinforcement distributions (for example Zywicz and Parks (1988), Levy and Papazian (1991), Tvergaard (1991), Povirk *et al.* (1992) and Weisbrook and Krawitz (1996)). In these studies, plastic flow is described either in terms of a classical continuum constitutive relation or in terms of a presumed arrangement of a relatively small number of discrete dislocations. While much insight has been gained from both descriptions, each has inherent limitations. The continuum description requires as input the *in-situ* stress–strain response of the matrix material, which is not necessarily the same as that of the matrix material in bulk. Furthermore, classical continuum plasticity predicts a size-independent response, whereas a dependence on reinforcement size is seen experimentally, for example by Nan and Clarke (1996). Conventional discrete dislocation approaches do predict a size effect, but assuming a dislocation structure avoids the issue of what dislocation structures evolve under a given set of conditions. In addition, the effect of reinforcement shape and distribution on composite behaviour is difficult to quantify within a conventional dislocation formulation.

In this paper, we present predictions of residual stresses in a simple model composite material using a discrete dislocation framework in which plastic flow arises directly from the collective motion of large numbers of discrete dislocations. Both the stress–strain response during unloading and the evolution of the dislocation structure are outcomes of the analysis. Full boundary value problems are solved and the effect of reinforcement morphology on composite response is illustrated.

As in the work of Van der Giessen and Needleman (1995) and Cleveringa *et al.* (1997, 1998), the focus is on the formulation and solution of boundary value problems for dislocated solids. The stresses and strains are written as superpositions of fields due to the discrete dislocations, which are singular inside the body, and image fields that enforce the boundary conditions and account for interaction with second-phase particles. Attention is restricted to small strains and the resulting linear elastic boundary value problem for the smooth image fields is solved by the finite-element method. Thus, the long-range interactions between dislocations are accounted for through the continuum elasticity fields. Drag during dislocation motion, interactions with obstacles, and dislocation nucleation and annihilation are also accounted for. These are not represented by the elasticity description of dislocations and are incorporated into the formulation through a set of constitutive rules, which are based on those proposed by Kubin *et al.* (1992). Recently, Polonsky and Keer (1996), Fivel *et al.* (1996) and Zacharopoulos *et al.* (1997) have presented particular boundary value problem solutions for dislocated solids using other methods to obtain image fields for large numbers of dislocations. An advantage of the finite-element method is its adaptability to rather general boundary value problems.

We consider the same model composite material as Cleveringa *et al.* (1997, 1998) did, namely a periodic distribution of particles subject to simple shear under plane strain conditions. Single slip is assumed on slip planes parallel to the shear direction. Attention is focused on three particle morphologies, as in the work of Cleveringa *et al.* (1997, 1998); in one case there are veins of unreinforced material between particles, while in the other two all slip planes are blocked by particles. Unloading from various pre-strains and for various reinforcement sizes is considered. For comparison purposes, the same boundary value problem is solved using a phenomenological continuum slip description of plastic flow (Peirce *et al.* 1983).

Experimentally, residual stresses in composites are inferred from X-ray or neutron diffraction measurements of lattice strains (Warren 1969; Noyan and Cohen 1987). The position of peaks in diffraction line profiles signify the mean lattice strain in a particular direction, while the breadth of the peak is correlated with the spatial distribution of the strain component. With this in mind, we compute the mean value and the variance of the residual strain distributions, on the basis of both the discrete dislocation and the continuum slip predictions.

§2. Problem formulation and method of analysis

The calculations are carried out for a two-dimensional model composite material containing elastic rectangular particles in a plastically deforming matrix. The particles are arranged in a doubly periodic hexagonal array as shown in figure 1. Each unit cell is of width $2w$ and height $2h$ $(w/h = \sqrt{3})$ and contains two particles of size $2w_f \times 2h_f$, one being located at the centre of the cell.

In the analyses, we assume small strains and rotations and the unit cell is subjected to plane-strain simple shear, which is prescribed through the boundary conditions

$$u_1(t) = \pm h\Gamma, \quad u_2(t) = 0 \quad \text{along } x_2 = \pm h, \tag{1}$$

where u_i are the displacement components and $\Gamma(t)$ is the applied shear at time t. Periodic boundary conditions are imposed along the lateral sides $x_1 = \pm w$. These kinematic boundary conditions somewhat constrain the deformation of the particles at the cell vertices (see figure 1). The average shear stress $\bar{\tau}$ needed to sustain the

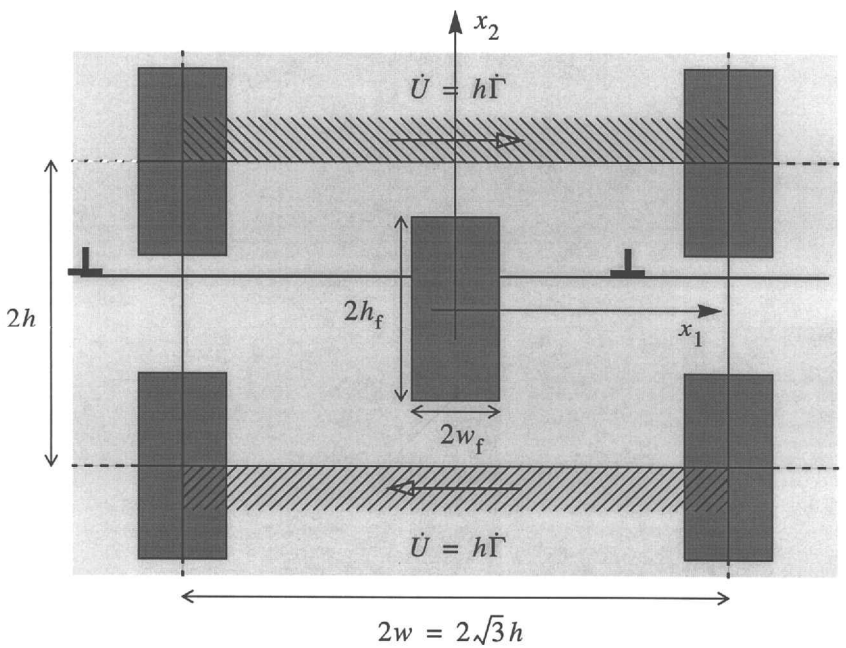

Figure 1. Unit cell of a composite material with a doubly periodic array of elastic particles. All slip planes are taken to be parallel to the applied shear direction (x_1).

deformation is computed from the shear component σ_{12} of the stress $\boldsymbol{\sigma}$, either along the top or the bottom face of the region:

$$\bar{\tau} = \frac{1}{2w} \int_{-w}^{w} \sigma_{12}(x_1, \pm h)\, \mathrm{d}x_1. \tag{2}$$

A positive $\dot{\Gamma}$ is imposed until a specified shear strain Γ is reached. Then, unloading is achieved by applying a negative $\dot{\Gamma}$ until the average shear stress $\bar{\tau}$ vanishes.

This problem is analysed by two computational methods: one in which dislocations are treated as discrete entities (singularities) in an elastic background material, while the other is a standard continuum slip crystal plasticity description.

2.1. *Discrete dislocation formulation*

The discrete dislocation formulation follows that of Van der Giessen and Needleman (1995) and Cleveringa *et al.* (1997) where the general development is given together with further references. The dislocations are treated as line defects in the elastic continuum (for example Nabarro (1967) and Hirth and Lothe (1968)) and the computation of the deformation history is carried out in an incremental manner. Each time step involves three main computational stages:

(i) determining the current stress and strain state for the current dislocation arrangement;
(ii) Determining the forces on the dislocations, that is the Peach–Koehler force;
(iii) determining the rate of change in the dislocation structure, which involves the motion of dislocations, the generation of new dislocations, their mutual annihilation, and their pinning at obstacles.

The method for determining the current state of the body with the current dislocation distribution is an extension of the formulation by Lubarda *et al.* (1993). The key idea is that each incremental step, the displacement, strain and stress fields are written as the superposition of two fields; for example $\boldsymbol{\varepsilon} = \tilde{\boldsymbol{\varepsilon}} + \hat{\boldsymbol{\varepsilon}}$ for the strain field $\boldsymbol{\varepsilon}$. The fields denoted by a tilde are the superposition of the fields of the individual dislocations, in their current configuration, but in an infinite medium of the homogeneous matrix material.

The fields denoted by a hat represent the image fields that correct for the actual boundary conditions and for the presence of the particles. The elastic moduli in each phase are taken to be isotropic, with shear modulus μ and Poisson's ratio υ in the matrix, and shear modulus μ^* and Poisson's ratio υ^* in the reinforcement.

For the plane-strain shear problem here, the boundary conditions for the fields denoted by a hat are

$$\hat{\mathbf{u}} = \mathbf{u} - \tilde{\mathbf{u}} \text{ along } x_2 = \pm h, \tag{3}$$

together with symmetry conditions along $x_1 = \pm w$. In equation (3), $\mathbf{u}$ is the prescribed displacement vector from equation (1). The fields denoted by a hat are smooth, so that the boundary value problem for them can be conveniently solved by the finite-element method. Here, the finite-element discretization used 102×60 four-node quadrilateral elements with 2×2 Gaussian integration.

We consider glide on a single slip system, with the slip plane normal $\mathbf{n}$ being in the x_2 direction and with the glide direction $\mathbf{m}$ being in the x_1 direction. Only edge dislocations are considered, all having the same Burgers vector magnitude b so that the Peach–Koehler force f^i on the ith dislocation is simply $f^i = \sigma^i_{12} b$, with σ^i_{12} being

the shear component of $\sigma = \tilde{\sigma} + \hat{\sigma}$ at the position of dislocation i. In calculating the $\tilde{\sigma}$ contribution to the Peach–Koehler force, the stress fields due to replicas of each dislocation in the unit cell in all other cells must be accounted for, which is accomplished as described by Van der Giessen and Needleman (1995).

The magnitude of the glide velocity v^i of dislocation i is taken to be linearly related to the Peach–Koehler force through the drag relation

$$f^i = Bv^i, \tag{4}$$

where B is the drag coefficient. The value of B is specified by the time constant $B/\mu = 0.38 \times 10^{-14}$ s, taking $\mu = 0.26 \times 10^5$ MPa and $B = 10^{-4}$ Pa s as representative parameter values for aluminium (Kubin *et al.* 1992). The elastic reinforcement is characterized by $\mu^* = 7.3\mu$ and $\upsilon^* = 0.17$, which is representative for silicon carbide particles in an aluminium matrix.

Obstacles to dislocation motion are modelled as fixed points on a slip plane. Such obstacles account for the effects of small precipitates or for dislocations on other secondary slip systems in blocking slip on the primary slip plane. Pinned dislocations can only pass the obstacles when their Peach–Koehler force exceeds an obstacle dependent value $\tau_{\text{obs}}b$. All obstacles are taken to have the strength $\tau_{\text{obs}} = 5.7 \times 10^{-3}\mu$.

Annihilation of two dislocations with opposite Burgers vector occurs when they are sufficiently close together. This is modelled by eliminating two dislocations when they are within a material-dependent critical annihilation distance L_{e}, which is taken to be $L_{\text{e}} = 6b$.

New dislocation pairs are generated by simulating Frank–Read sources. In two dimensions, with single slip, this is simulated by point sources on the slip plane which generate a dislocation dipole when the magnitude of the Peach–Koehler force at the source exceeds the critical value $\tau_{\text{nuc}}b$ during a period of time t_{nuc}. The distance L_{nuc} between the dislocations is specified as

$$L_{\text{nuc}} = \frac{\mu}{2\pi(1-\upsilon)}\frac{b}{\tau_{\text{nuc}}}. \tag{5}$$

At this distance, the shear stress of one dislocation acting on the other is balanced by the slip plane shear stress. The magnitude of τ_{nuc} is randomly chosen from a Gaussian distribution with mean strength $\bar{\tau}_{\text{nuc}} = 1.9 \times 10^{-3}\mu$ and standard deviation of $0.2\bar{\tau}_{\text{nuc}}$. With $\upsilon = 0.3$, this mean nucleation strength corresponds to a mean nucleation distance of $L_{\text{nuc}} = 125b$ and amounts to 30% of the obstacle strength τ_{obs}. The nucleation time for all sources is taken as $t_{\text{nuc}} = 2.6 \times 10^6 B/\mu$.

As in the work of Cleveringa *et al.* (1997), most calculations used an adaptive time-stepping procedure which ensured that all nucleation events were captured accurately and that all increments of dislocation glide remained within specified margins. As a consequence, the number of time steps required was very large. Some computations used a fixed time step $\Delta t = 0.05t_{\text{nuc}} = 1.3 \times 10^5 B/\mu$, which is three orders of magnitude larger than the smallest steps in the adaptive procedure. The loading responses thus obtained were not identical with those with the adaptive procedure but the difference is mainly in the oscillations about the mean stress–strain response.

2.2. *Continuum slip formulation*

For comparison purposes, the same problem is solved using a continuum slip formulation, again assuming small displacement gradients. Overviews of the continuum slip formulation and its physical background have been given by Asaro (1983), Cuitiño and Ortiz (1992) and Bassani (1994). Here, there is one slip system with the slip plane normal $\mathbf{n}$ parallel to the x_2 axis and with the slip direction $\mathbf{m}$ parallel to the x_1 axis. The total strain rate $\dot{\boldsymbol{\varepsilon}}$ is written as the sum of an elastic part and a plastic part. The elastic strain rate $\dot{\boldsymbol{\varepsilon}}^{\mathrm{e}}$ is given in terms of the stress rate $\dot{\boldsymbol{\sigma}}$ by Hooke's law and the plastic strain rate $\dot{\boldsymbol{\varepsilon}}^{\mathrm{p}}$ is given by

$$\dot{\boldsymbol{\varepsilon}}^{\mathrm{p}} = \dot{\gamma}\,\mathrm{sym}\,(\mathbf{m} \otimes \mathbf{n}) \tag{6}$$

(sym denoting the symmetric part of a tensor) with $\dot{\gamma}$ given by the power-law relation

$$\dot{\gamma} = \dot{a}\,\frac{\tau}{g}\left(\left|\frac{\tau}{g}\right|\right)^{1/m-1}. \tag{7}$$

Here, $\dot{a}$ is a reference strain rate, m is the strain rate hardening exponent, g is the slip system hardness, and the slip system resolved shear stress τ is σ_{12}. In all calculations here, $\dot{a}/\dot{\Gamma} = 0.5$ and $m = 0.005$. The slip system strain hardening is described by

$$g(\gamma) = \tau_0 + \frac{\gamma_0 h_0}{N}\left[\left(\frac{\gamma}{\gamma_0}+1\right)^{N} - 1\right], \tag{8}$$

where τ_0 is the slip system strength, γ_0 is a reference strain, h_0 is the initial hardening rate and N is the strain-hardening exponent.

The continuum slip finite-element discretization is based on quadrilateral elements consisting of four 'crossed' linear displacement triangles. This type of element is used in order to avoid locking problems associated with incompressible plastic deformations. The same 102×60 quadrilateral mesh is used as in the discrete dislocation calculations. The unit cell is subject to the boundary conditions (1) together with periodicity at $x_1 = \pm w$, and the deformation history is calculated in a linear incremental manner. In order to increase the stable time step, the rate tangent modulus method of Peirce *et al.* (1983) is used for the time integration.

§3. Results

As in the work of Cleveringa *et al.* (1997), a fixed density of active slip planes is considered in the simulations, corresponding to an active slip plane spacing of $100b$. Three reinforcement morphologies are considered:

(i) square particles $(h_{\mathrm{f}} = w_{\mathrm{f}})$ with an area fraction of 0.2, that is $h_{\mathrm{f}} = 0.416h$;
(ii) square particles $(h_{\mathrm{f}} = w_{\mathrm{f}})$ with an area of fraction 0.289, that is $h_{\mathrm{f}} = 0.5h$;
(iii) particles with $h_{\mathrm{f}} = 2w_{\mathrm{f}}$ with an area fraction of 0.2, that is $h_{\mathrm{f}} = 0.588h$.

These three morphologies are referred to as material (i), material (ii) and material (iii) respectively. Material (i) represents a material with square particles in which the density of reinforcing particles is low enough that veins of unreinforced material remain. With the higher area fraction of square particles in material (ii), all slip planes are cut by particles. Material (iii) has the same area fraction of particles as material (i), but because of the particle shape there are no unreinforced veins. The size scale of the microstructure is set by the height h of the unit cell relative to the

material length scale L which is specified in terms of the Burgers vector as $L = 4000b$. The reference cell size is $h = L$ (with $b = 2.5 \times 10^{-10}$ m as a representative value, the length $L = 1$ μm so that the cell has dimensions 3.46 μm by 2 μm). Size effects are considered for material (iii) by taking $h = L/2$ and $h = 2L$.

3.1. *Response to unloading*

In the initial undeformed state the matrix is dislocation free. Dislocation sources and obstacles are randomly distributed in the matrix (their locations are shown subsequently). The density of dislocation sources is taken to be the same as the density of dislocation obstacles, with the values $61.2L^{-2}$, $46.2L^{-2}$ and $55.4L^{-2}$, for materials (i), (ii) and (iii) respectively. Forward shear loading is imposed to a specified strain and then the specimen is unloaded. The applied shear rate enters through the dimensionless number $B\dot{\Gamma}/\mu = 0.38 \times 10^{-11}$; with the parameter values used here this corresponds to a shear rate of $\dot{\Gamma} = \dot{\Gamma}_0 = 10^3\ \mathrm{s}^{-1}$. The overall stress responses predicted by the discrete dislocation model (figure 2) are then used to fit the hardening parameters of the continuum slip constitutive relation, and we find the following: $\gamma_0 = 0.01$, $N = 0.1$, $(\gamma_0 h_0)/(N\tau_0) = 1.43$ and $\tau_0/\mu = 5.3 \times 10^{-4}$ for material (i); $\gamma_0 = 0.002$, $N = 1.0$, $(\gamma_0 h_0)/(N\tau_0) = 1.76 \times 10^{-2}$ and $\tau_0/\mu = 1.12 \times 10^{-3}$ for material (ii); $\gamma_0 = 0.002$, $N = 1.0$, $(\gamma_0 h_0)/(N\tau_0) = 3.77 \times 10^{-2}$ and $\tau_0\mu = 1.31 \times 10^{-3}$ for material (iii). The discrete dislocation simulation of material (i) predicts softening after yield due to localization of flow in the unreinforced veins. However, a weakly hardening response is used in the continuum calculations (in order to avoid numerical issues associated with plastic flow localization). Materials (ii) and (iii) show linear hardening (Cleveringa *et al.* 1997).

Then, from a pre-strain $\Gamma = 0.58\%$, the materials are unloaded by reverse shearing $(\dot{\Gamma} < 0)$ until a macroscopically stress-free state, $\bar{\tau} = 0$, is reached. Material (iii) is also unloaded from a pre-strain $\Gamma = 0.96\%$. Figure 2 shows the predicted stress–strain curves when unloading is carried out at the same rate as loading $(|\dot{\Gamma}| = \dot{\Gamma}_0)$. While the continuum model predicts essentially elastic unloading, the discrete dislocation model predicts inelastic behaviour rather soon after the beginning of unloading. This is clearest for materials (ii) and (iii) (figures 2(*b*) and (*c*)), where residual plastic strains of the order of 0.15% are found. In material (i), shown in figure 2(*a*), reverse plastic straining also occurs but is less noticeable because of the lower stress levels.

The occurrence of reverse plastic flow is evidence of substantial dislocation activity during unloading. According to the evolution of the dislocation density shown in figure 3, this involves not only dislocation motion but also significant annihilation. During the first 0.05% of reverse straining, the dislocation densities remain constant, but subsequently they decrease in an almost linear fashion for materials (ii) and (iii). In both materials, the rate of annihilation of mobile (i.e. unpinned) dislocations is slightly smaller than that of the total number of dislocations, indicating that also the previously pinned dislocations are being annihilated. Here, the mobile dislocations are defined to be those that are not pinned at obstacles and therefore are able to move according to equation (4).

In order to get some insight into the dislocation processes during unloading, figures 4–6 show the dislocation distributions in the three materials at the start of unloading and in the unloaded state, at $\bar{\tau} = 0$. Figure 4(*a*) shows that the forward shearing of material (i) leads to planar arrays of dislocations in between the particles with a strong tendency for dipole formation. In the unloaded state, shown in

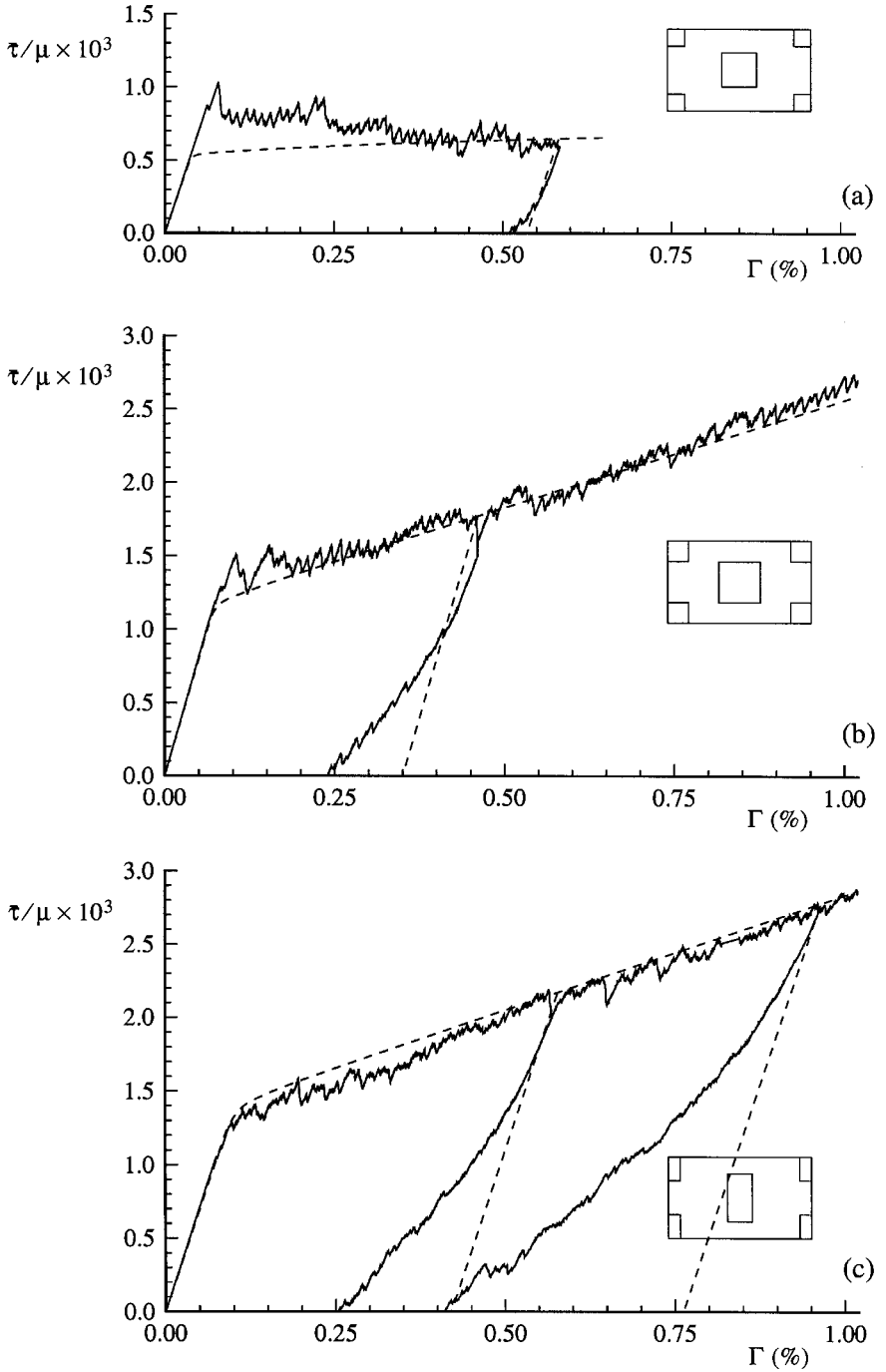

Figure 2. Curves of shear stress against shear strain for forward shearing and unloading from some shear strain to $\bar{\tau} = 0$ according to the discrete dislocation model (—) and according to the continuum description (- - - -): (*a*) material (i); (*b*) material (ii); (*c*) material (iii). For all materials, unloading from around $\Gamma = 0.58\%$ is shown while, for material (iii), unloading from $\Gamma = 0.96\%$ is also shown.

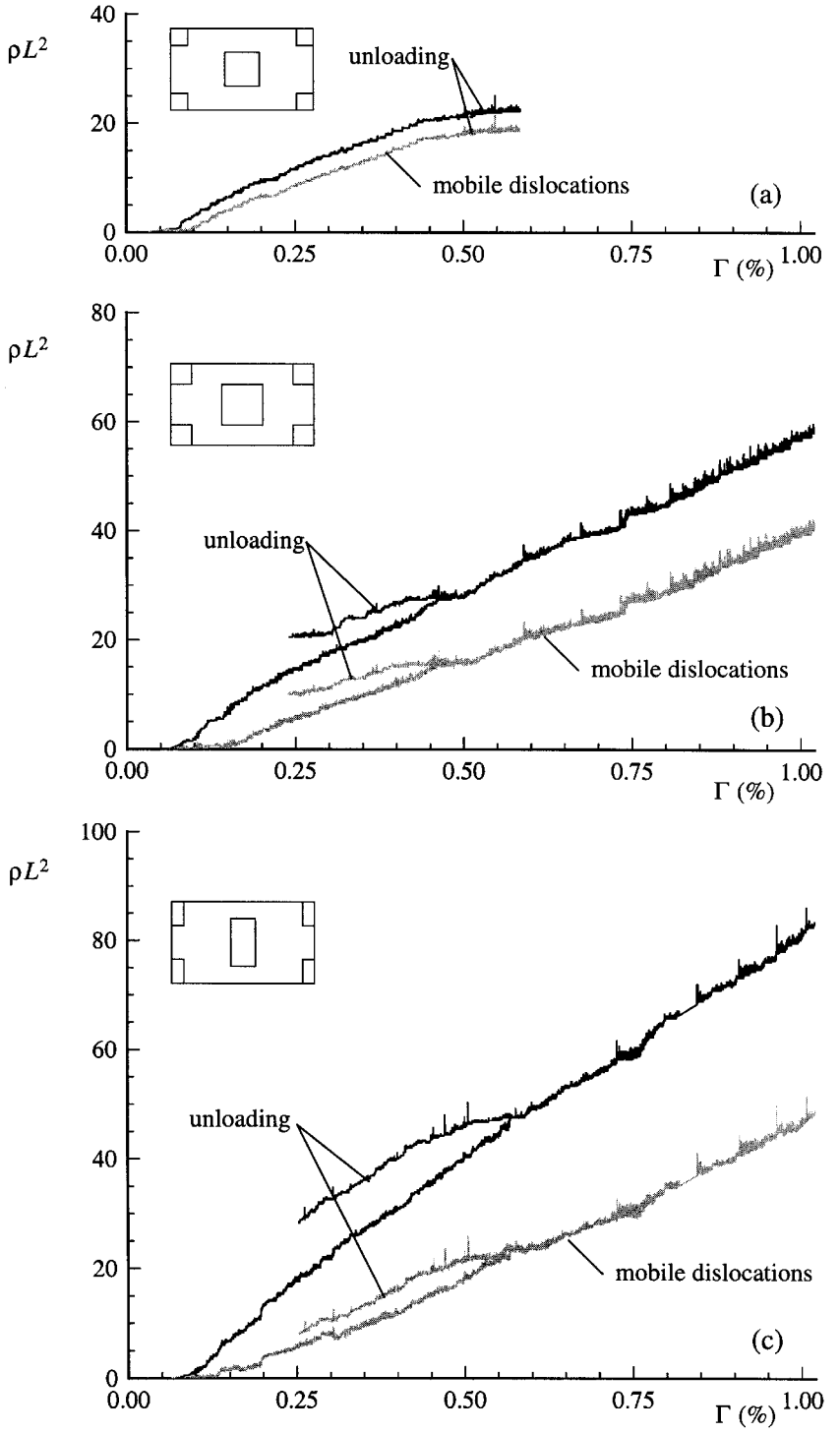

Figure 3. Evolution of dislocation density ρ during loading and during unloading $\bar{\tau} = 0$: (*a*) material (i); (*b*) material (ii); (*c*) material (iii). The grey curve, labelled mobile dislocations, shows the evolution of all dislocations that are not pinned at obstacles.

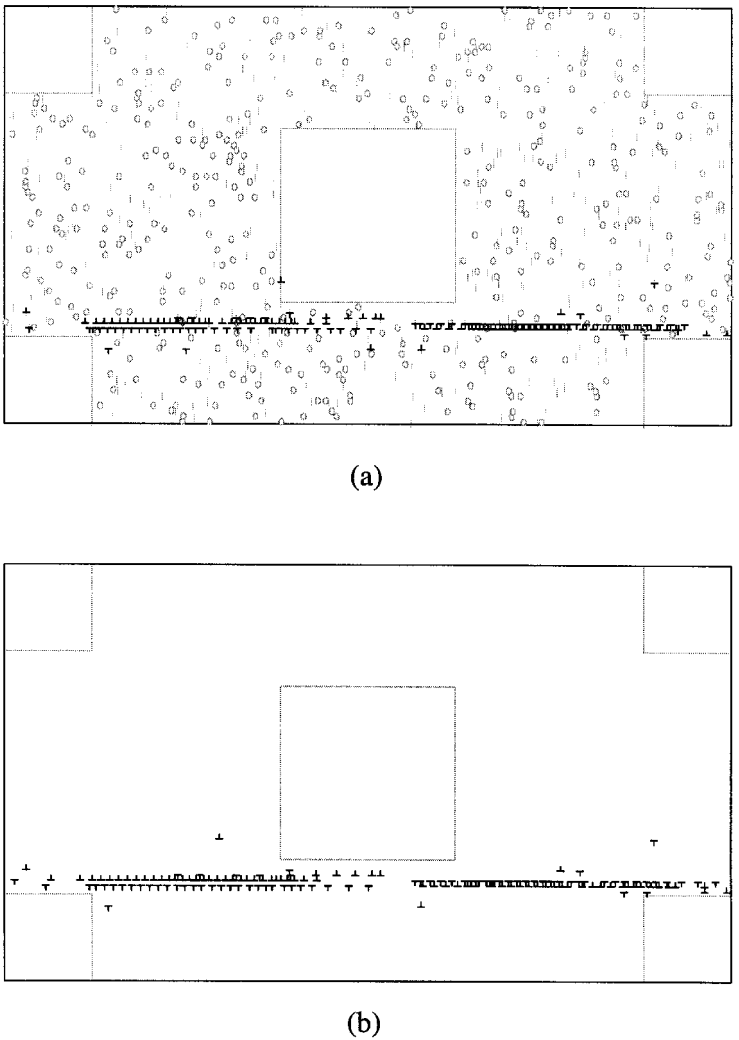

Figure 4. Dislocation distribution in material (i): (*a*) at $\Gamma = 0.58\%$ during loading; (*b*) after unloading to $\bar{\tau} = 0$. The grey open circles and vertical bars in (*a*) indicate the sources and obstacles respectively.

figure 4(*b*) this dislocation structure is largely unchanged. In material (ii), where all slip planes are blocked by particles, dislocations tend to pile up against the particles, preferably near the particle corners where this leads to long dislocation pile-ups (figure 5(*a*)). After unloading (figure 5(*b*)), these long pile-ups have dissolved to a large extent. In material (iii), more significant piling up against the particles is seen during shearing (figure 6(*a*)), which was interpreted by Cleveringa *et al.* (1997) in terms of geometrically necessary dislocations. Again, after unloading, the pile-ups have dissolved to some extent, thus leaving a rather homogeneous dislocation distribution (figure 6(*b*)).

From these observations, the following picture emerges: on unloading, the Peach–Koehler forces due to the correction stresses $\hat{\boldsymbol{\sigma}}$ quickly reduce. At some

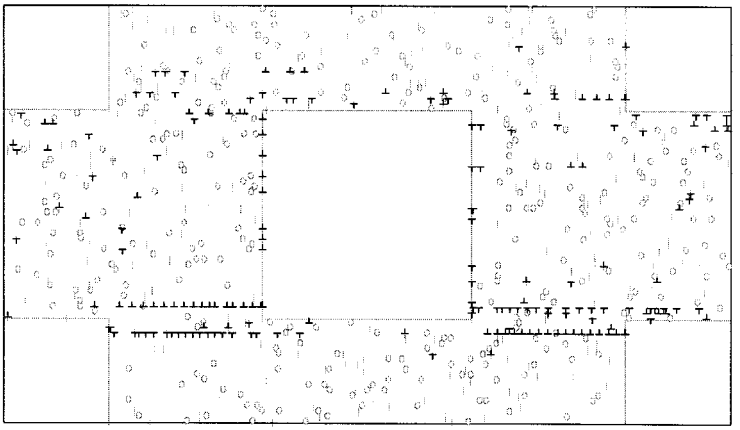

(a)

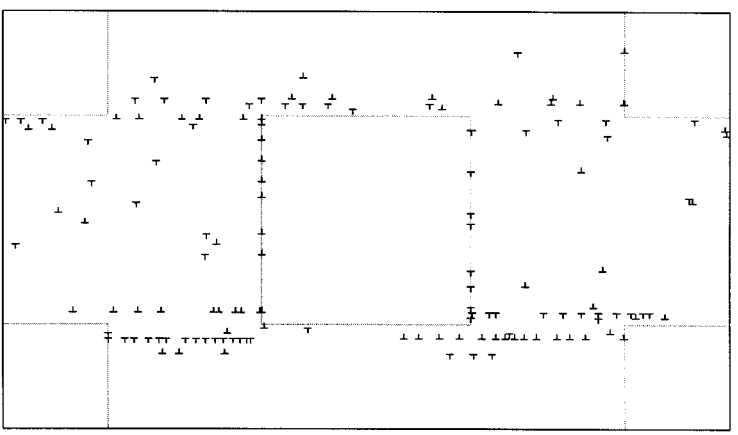

(b)

Figure 5. Dislocation distribution in material (ii); (*a*) at $\Gamma = 0.46\%$ during loading; (*b*) after unloading to $\bar{\tau} = 0$. The grey open circles and vertical bars in (*a*) indicate the sources and obstacles respectively.

point, this changes the sign of the total Peach–Koehler force at some dislocations, so that the mobile dislocations reverse direction. When they have moved over sufficiently large distances, the mobile dislocations meet dislocations of opposite sign and annihilate. The sign change of the Peach–Koehler force will occur rather quickly in a dislocation pile-up because of the high internal stresses due to the dislocation–dislocation interaction.

This interpretation implies that the relaxation behaviour is strongly affected by the dislocation mobility relative to the imposed strain rate, as governed by the dimensionless number $B\dot{\Gamma}/\mu$. This is explored further by repeating the unloading simulations for material (iii) with strain rates $|\dot{\Gamma}|$ that are up to three orders of magnitude larger than $\dot{\Gamma}$. The results in figure 7 indeed show that the extent of

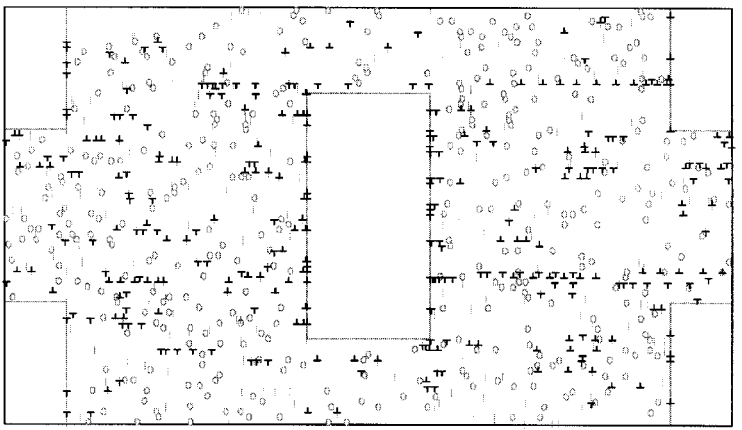

(a)

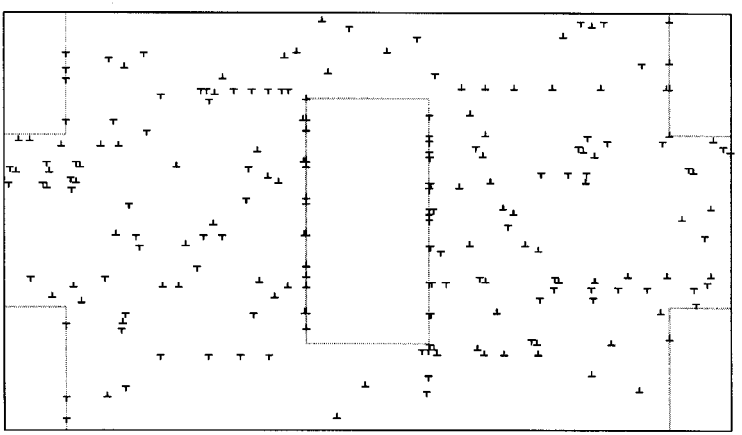

(b)

Figure 6. Dislocation distribution in material (iii): (*a*) at $\Gamma = 0.58\%$ during loading; (*b*) after unloading to $\bar{\tau} = 0$. The grey open circles and vertical bars (*a*) indicate the sources and obstacles respectively.

reverse plasticity decreases with increasing value of $|\dot{\Gamma}|$. At the higher rates, there is less time for dislocations to move and therefore to approach each other close enough to annihilate. However, the sensitivity to $B\Gamma/\mu$ is rather weak, so that a thousand-fold increase or more is necessary to eliminate reverse plasticity in the discrete dislocation simulations. Then, the unloading response approaches that predicted by the continuum slip model.

The dislocation structure resulting after rapid unloading is, however, frozen in and far from equilibrium, so that one expects that it will evolve with time in the unloaded state in order to relax the internal energy further. This is investigated by subsequent calculations where the average shear stress is kept zero. Because of the nature of the boundary conditions (1) used in the present calculations, this requires a

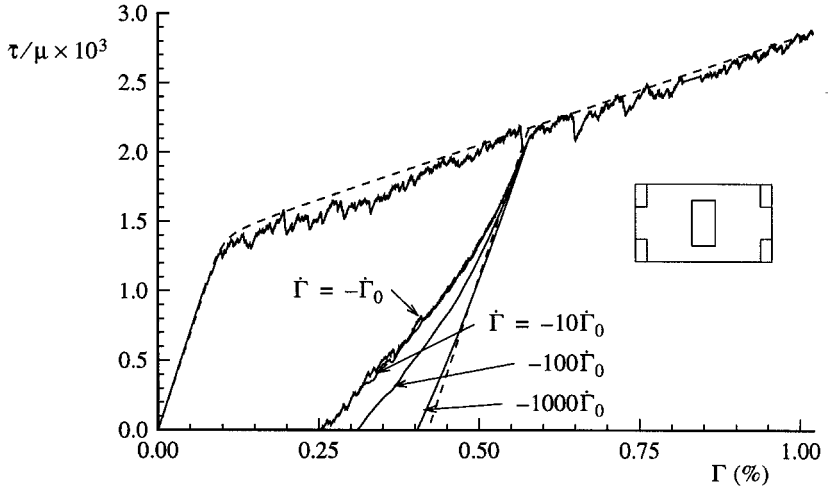

Figure 7. Effect of the shear rate during unloading on the shear stress response of material (iii). The continuum results (- - - -) during unloading are virtually insensitive to the shear rate.

special solution procedure that is described in appendix A. Figure 8, for material (iii) unloaded at $\dot{\Gamma} = -1000\dot{\Gamma}_0$, shows that relaxation involves significant recovery of the dislocation structure, with the dislocation density eventually approaching the same density as obtained during unloading at $\dot{\Gamma} = -\dot{\Gamma}_0$. In that state, the two dislocation distributions are almost identical (cf. figure 6(*b*)), with a few minor differences that can be attributed, at least in part, to stochastic effects. A similar relaxation analysis

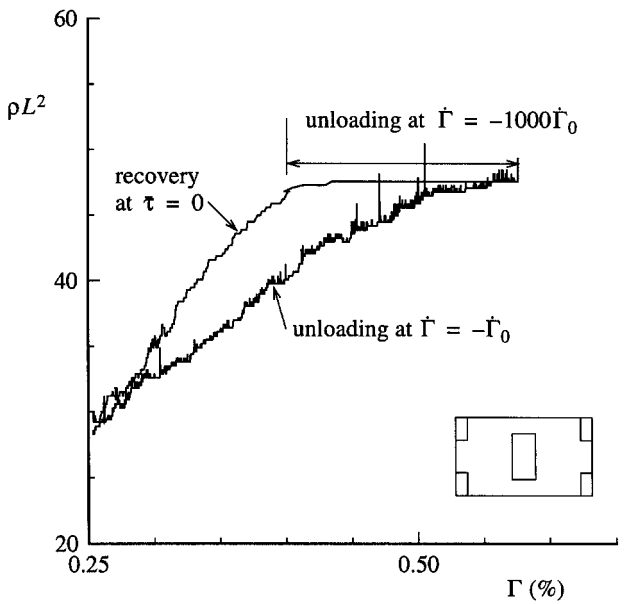

Figure 8. Evolution of dislocation density in material (iii) during rapid unloading from $\Gamma = 0.58\%$ followed by recovery under overall zero shear stress. The result for unloading at the reference strain rate $\dot{\Gamma}_0$ (cf. figure 3(*c*)) is shown for comparison.

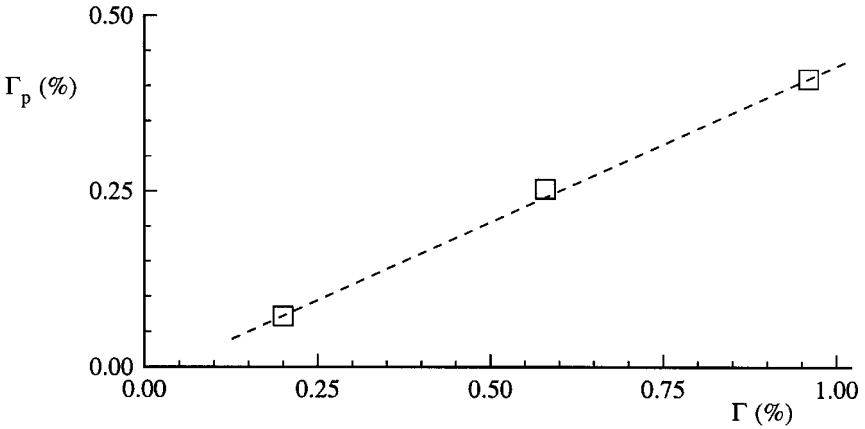

Figure 9. Residual plastic shear strain Γ_p in material (iii) after unloading with $\dot{\Gamma} = -\dot{\Gamma}_0$ from a pre-strain Γ.

has been carried out for material (iii) unloaded at $\dot{\Gamma} = -\dot{\Gamma}_0$, but we find a negligible change compared with the dislocation structure in figure 6(*b*).

Unloading calculations have also been carried out for material (iii) from pre-strains Γ of 0.2% and 0.96% (the latter will be discussed in more detail later). Figure 9 shows the resulting residual plastic strain Γ^p after unloading to $\bar{\tau} = 0$ with $\dot{\Gamma} = -\dot{\Gamma}_0$ as a function of pre-strain. Although there are only a few data points it appears that Γ^p increases linearly with increasing Γ over the range considered.

3.2. *Residual stresses*

After unloading, the materials contain residual stresses that are due to the presence of the elastic particles and the dislocations in the matrix. Figure 10 shows the distributions of the residual shear stress for materials (i) and (iii) in comparison with the residual stresses obtained using the continuum description. In either material, the residual stress fields in the matrix show the strong effect of the residual dislocations. The figure also demonstrates that the residual stresses in the particles in material (iii) are much larger than in material (i), even in the continuum model. Near the particle interfaces in material (iii), on both the matrix and the particle sides, there are strong stress peaks (figure 10(*b*)), which are associated with the dislocations that are left piled up against the particles.

The average values (denoted by angular brackets) of all residual stress components over the matrix are listed in table 1. The corresponding average residual stresses in the reinforcement (denoted by angular brackets with an asterisk) were also calculated and, to within 0.5% of the magnitude of the matrix residual shear stress, are consistent with overall equilibrium expressed by

$$f\langle\sigma_{ij}\rangle^* + (1-f)\langle\sigma_{ij}\rangle = \bar{\tau}. \tag{9}$$

The dominant residual stress clearly is the shear stress $\langle\sigma_{12}\rangle$. For material (i), where localization of deformation occurs in the discrete dislocation analysis, but not in the continuum slip analysis, the discrete dislocation analysis predicts a residual stress that is about three times larger than predicted by the continuum slip analysis. On the other hand, for material (iii) the residual stresses in this direction predicted by the

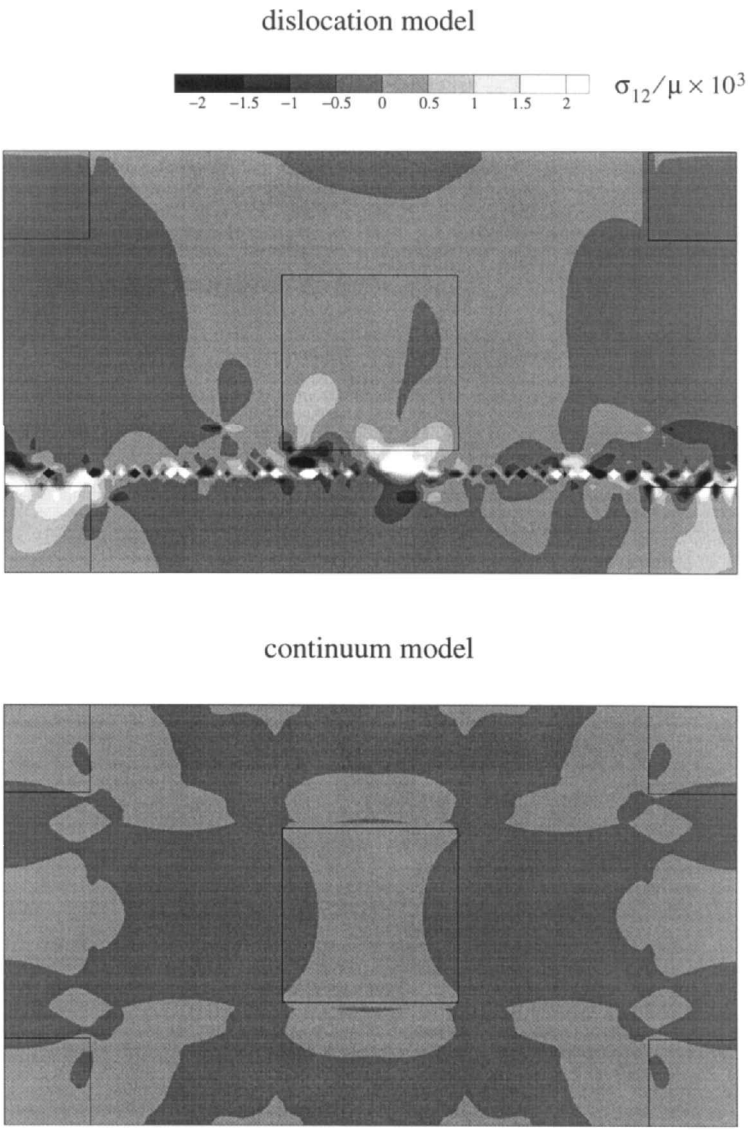

Figure 10. Comparison of residual shear stress distributions after unloading from $\Gamma = 0.58\%$ according to dislocation and continuum slip model: (*a*) material (i) (cf. figure 4 (*b*)); (*b*) material (iii) (cf. figure 6 (*b*)).

two formulations are within 35% of each other, with the continuum slip analysis predicting somewhat larger residual stresses. However, the overall residual plastic strains predicted by the two formulations are very different so that a quantitative comparison is not appropriate.

The overall shear stress values $\bar{\tau}$ from which unloading took place are $0.5 \times 10^{-3}\mu$ for material (i), $2.0 \times 10^{-3}\mu$ for material (iii) at $\Gamma = 0.58\%$, and

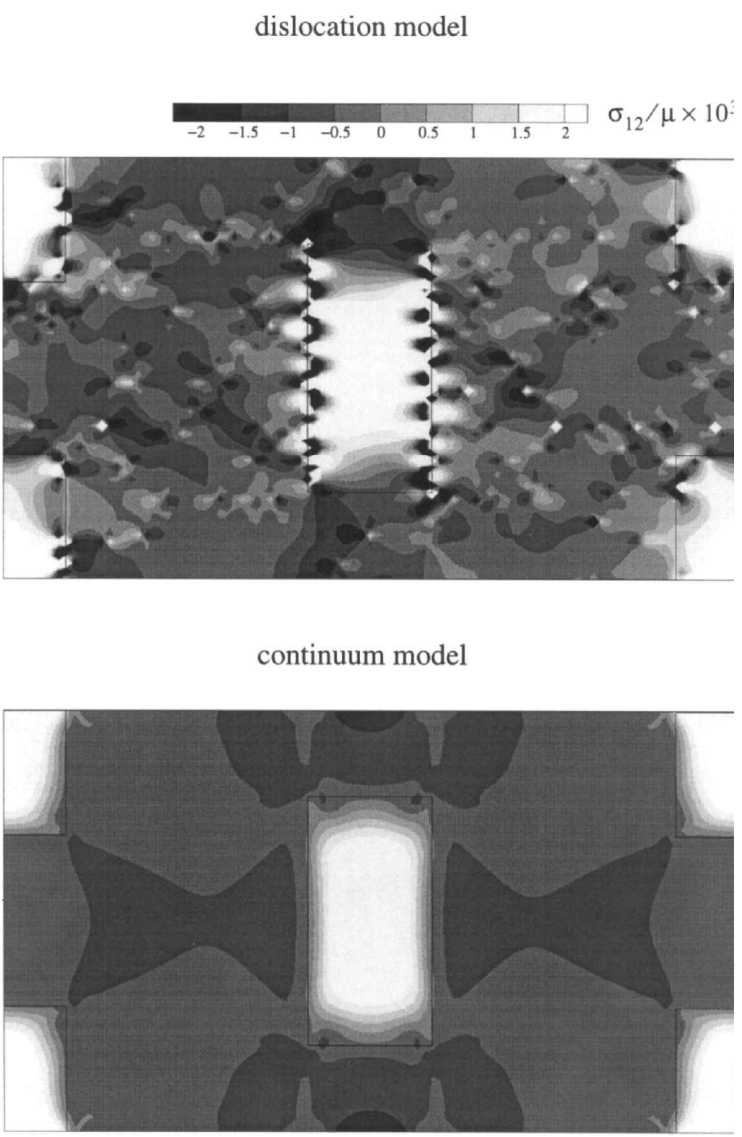

Figure 10

$2.8 \times 10^{-3}\mu$ for material (iii) at $\Gamma = 0.96\%$ (see figures 2(*a*) and (*c*)). Hence, the matrix residual shear stresses predicted for material (iii) are about 20% of the overall shear stress at the onset of unloading. The residual matrix shear stress for material (i) is significantly less, being about 10% of the overall value at the onset of unloading according to the discrete dislocation formulation and a factor of three smaller according to the continuum slip prediction. The other stress components in table 1 are more than an order of magnitude smaller than the matrix residual shear stress

Table 1. Matrix residual stresses.

Material	Γ (%)	$\langle\sigma_{11}\rangle/\mu \times 10^6$	$\langle\sigma_{22}\rangle/\mu \times 10^6$	$\langle\sigma_{12}\rangle/\mu \times 10^6$
(i) dislocation	0.58	−2.2	−0.48	−55.5
(i) continuum	0.58	0.36	0.62	−17.3
(iii) dislocation	0.58	−1.6	1.2	−380
(iii) continuum	0.58	1.3	1.3	−418
(iii) dislocation	0.96	4.4	−4.7	−586
(iii) continuum	0.96	3.7	3.6	−824

and have comparable magnitudes for the two formulations (but not necessarily the same sign), with the exception of the $\langle\sigma_{11}\rangle$ stress for material (i).

A central justification for a continuum description of slip is that the representative volume element contains sufficiently many dislocations that the fields caused by the individual dislocations become 'smeared out'. However, the actual scale transition from dislocation-controlled to continuum-controlled behaviour has not been made explicit so far. As in the work of Cleveringa *et al.* (1997), we address this issue by considering averages of the shear stress fields in the matrix over windows of various sizes. The largest relevant window is equal to the entire matrix area of the unit cell. On gradually reducing the size of the windows, spatial distributions in the stress distribution become resolved with increasing accuracy. The bar charts depicted in figure 11 give a summary of the window-averaged residual shear stresses for materials (i) and (iii), both unloaded from $\Gamma = 0.58\%$. The bar charts are produced by computing the minimum and maximum value of $\langle\sigma_{12}\rangle$, and plotting these values in a bar against the ratio of the window area A_w to the total matrix area A_m. Thus, these plots show how the range of values $\langle\sigma_{12}\rangle$ gradually shrinks as the area over which it is averaged is increased. One of the most striking features is that the dislocation-based bar charts are much wider than those obtained from the continuum slip model. This is to be attributed to the stress fields caused by the individual dislocations; at the window sizes considered here, there are not enough dislocations per window that the individual singular fields cancel out.

3.3. *Residual strains*

Experimentally, residual stresses in composites can be inferred from X-ray and neutron diffraction measurements, as for example in the work of Tsai *et al.* (1981), Krawitz *et al.* (1988), Allen *et al.* (1992) and Povirk *et al.* (1992). What is measured, for both types of radiation, is the spacing between lattice planes (Warren 1969, Noyan and Cohen 1987). Then, if the lattice spacing in a stress-free reference state is known, the strain components can be calculated. Residual stresses are calculated from these residual strain values using the elastic moduli.

Because of the short penetration depth of X-rays in the materials of interest for metal-matrix composites, X-ray diffraction studies have generally focused on surface behaviour. The greater penetration depth of neutrons makes them attractive for bulk studies, but limitations of spatial resolution generally confine the results for metal-matrix composites to phase averages.

Thus, for comparison with neutron diffraction residual strain measurements, the quantities of interest are the phase-averaged 'lattice' strains along various lattice directions. For the two-dimensional model composite analysed here, we imagine

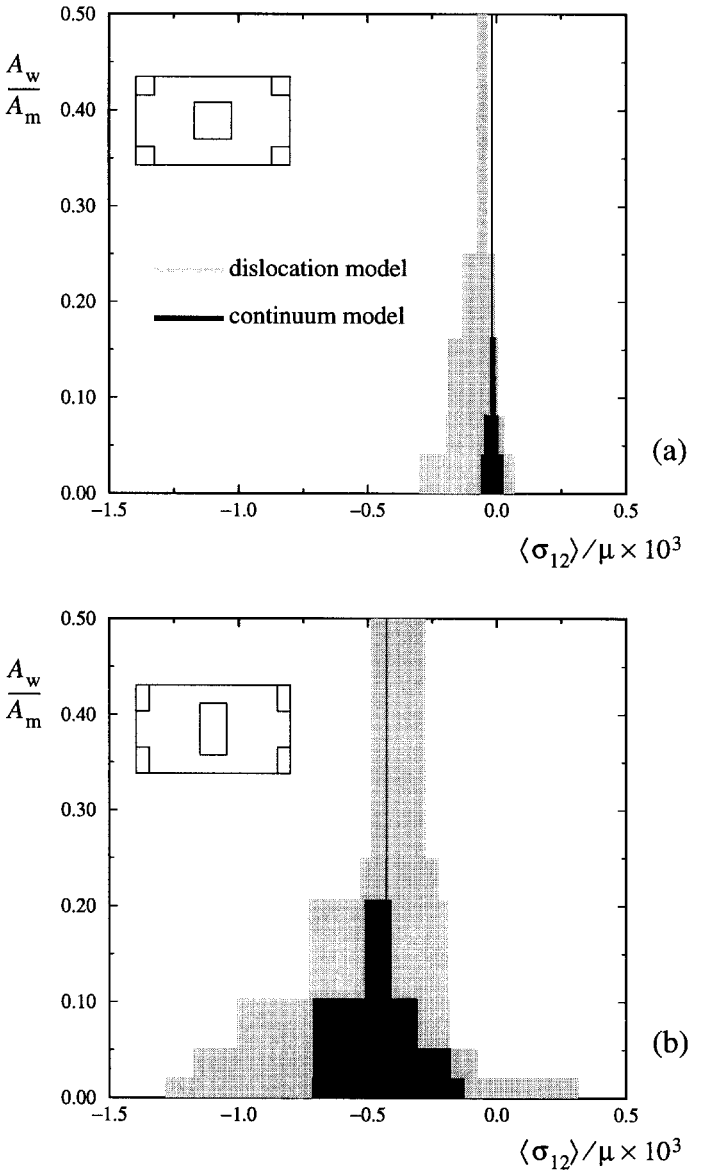

Figure 11. Bar chart of window-averaged residual shear stresses in the matrix after unloading from $\Gamma = 0.58\%$ according to dislocation and continuum slip model: (*a*) material (i); (*b*) material (iii) (cf. figure 10).

that the matrix has a square crystal structure with axes parallel to the coordinate axes. Using two-dimensional Miller index notation, we refer to strains along various lattice directions by $\varepsilon_{[hk]}$. This is the strain component that corresponds to the change in spacing between $\{hk\}$ planes. In the discrete dislocation model, the 'lattice' strains correspond directly to the total strain field $\boldsymbol{\varepsilon} = \bar{\boldsymbol{\varepsilon}} + \hat{\boldsymbol{\varepsilon}}$, whereas in the continuum slip formulation they correspond to the elastic part $\boldsymbol{\varepsilon}^e$ of the continuum strain. In either case, the 'lattice' strain tensor is conveniently calculated from the stress field as $\boldsymbol{\mathcal{L}}^{-1} : \boldsymbol{\sigma}$.

Table 2. Average 'lattice' strains in the matrix, obtained with 5×5 trapezoidal quadrature and a cut-off radius of $6.9b$ in the dislocation computations.

Material	Γ (%)	$\langle\varepsilon_{[hk]}\rangle \times 10^6$ for the following hk		
		10	11	01
(i) dislocation	0.58	−0.504	−29.7	−0.238
(i) continuum	0.58	0.0181	−8.57	0.147
(iii) dislocation	0.58	−1.07	−195	1.09
(iii) continuum	0.58	0.230	−209	0.224
(iii) dislocation	0.96	2.72	−294	−2.51
(iii) continuum	0.96	0.631	−411	0.603

One issue is how the discrete dislocation and continuum slip predictions compare for these strains. Table 2 shows such a comparison of the average matrix residual strains along the [10], [11] and [01] directions in three cases: material (i) unloaded from a pre-strain of 0.58%; material (iii) unloaded from a pre-strain of 0.58%; material (iii) unloaded from a pre-strain of 0.96%. The [10], [11] and [01] directions are parallel to the shearing direction, at 45° to the shearing direction and perpendicular to the shearing direction respectively. The main residual strain is, as expected, at 45° to the shearing direction. The comparison between the discrete dislocation and continuum slip values exhibits the same trends as seen for the residual stresses in table 1.

The matrix-averaged residual strains in table 2 for the discrete dislocation analyses involves integrating both the $\tilde{\varepsilon}_{[hk]}$ and $\hat{\varepsilon}_{[hk]}$ fields over each finite element. The $\tilde{\varepsilon}_{[hk]}$ fields have a $1/r$ singularity associated with each dislocation, but these singularities are integrable so that there is a well defined value for the average strain components. The values presented here were obtained using 5×5 trapezoidal quadrature to calculate the area integral over each finite element. A cut-off radius of $6.9b$ was used in the sense that, if a dislocation was located closer than this distance to an integration point, the strain was capped at the cut-off radius value. The number of integration points per element, the value of the cut-off radius and the integration scheme (Gaussian as well as trapezoidal) were varied. The matrix-averaged residual strains for the continuum slip calculations are essentially independent of the integration scheme. For the discrete dislocation cases, better convergence was found with the trapezoidal scheme owing to the dislocation strain singularity, with the slowest convergence occurring for the $\langle\varepsilon_{[01]}\rangle$ and $\langle\varepsilon_{[10]}\rangle$ values for material (i). Evidently, the highly localized dislocation arrangement that develops for material (i) presents numerical difficulties for a simple integration scheme. Nevertheless, all the integration schemes for that case give values of $\langle\varepsilon_{[01]}\rangle$ and $\langle\varepsilon_{[10]}\rangle$ that are more than an order of magnitude smaller than $\langle\varepsilon_{[11]}\rangle$.

In addition to the phase-average strains $\langle\varepsilon_{[hk]}\rangle$ we consider the strain variance defined by

$$\Psi(\varepsilon_{[hk]}) = \langle(\varepsilon_{[hk]} - \langle\varepsilon_{[hk]}\rangle)^2\rangle = \langle\varepsilon_{[hk]}^2\rangle - \langle\varepsilon_{[hk]}\rangle^2. \tag{10}$$

The strain variance is of interest because it provides a contribution to the broadening of the diffraction line. An approximate analysis of Stokes and Wilson (1944) gives that the line broadening is proportional to the standard deviation $[\Psi(\varepsilon_{[hk]})]^{1/2}$. While the connection between the variance of the strain and line breadth is not rigorous,

Table 3. Standard deviation of the 'lattice' strain in the matrix, obtained with 5×5 trapezoidal quadrature and a cut-off radius of $6.9b$ in the dislocation computations.

Material	Γ (%)	$[\Psi(\varepsilon_{[hk]})]^{1/2} \times 10^3$ for the following hk		
		10	11	01
(i) dislocation	0.58	0.661	0.461	0.358
(i) continuum	0.58	0.080	0.034	0.073
(iii) dislocation	0.58	0.863	0.685	0.589
(iii) continuum	0.58	0.527	0.240	0.666
(iii) dislocation	0.96	1.21	0.877	0.863
(iii) continuum	0.96	0.961	0.405	1.20

deviations from a uniform strain state do contribute to broadening (for example Krawitz *et al.* (1988)), since a uniform strain state gives rise to a mathematically sharp diffraction line. There are, of course, other contributions to diffraction line broadening and the relative importance of the contribution due to a non-zero strain variance remains to be quantified in specific circumstances. Nevertheless, a comparison of the strain variance predicted by continuum slip plasticity with that predicted by the discrete dislocation formulation provides an assessment of the contribution of the mesoscopic strain fluctuations due to discrete dislocations to line broadening.

Table 3 shows the values of the strain standard deviation $\Psi^{1/2}$ obtained using 5×5 trapezoidal quadrature and a cut-off radius of $6.9b$. Calculating the strain variance in equation (10) requires evaluating $\langle \varepsilon^2_{[hk]} \rangle$ which, because of the discrete dislocation strain singularity, requires integrating terms of the order of $1/r^2$. These terms diverge and the values of the strain variance inherently depend on the cut-off radius used. For example, with 4×4 Gaussian quadrature, varying the cut-off radius between $4b$ and $6.9b$ gave rise to changes in $\Psi(\varepsilon_{[hk]})$ of up to 40%. The largest variation was found in the values in the [11] direction.

For all cases in table 3, the discrete dislocation predictions for the variance of the [11] strain component is higher than the corresponding continuum slip prediction, even though in two of these cases the mean value obtained from the discrete dislocation formulation is lower. Although the actual value of the strain variance depends on the integration scheme and the cut-off distance used, the increased [11] strain variance provides a measure of the increased heterogeneity of the strain field associated with the discrete dislocations.

3.4. *Size effects*

Cleveringa *et al.* (1997) showed that the discrete dislocation model predicts a significant effect of particle size on the overall response during shearing. This was later explored in more detail (Cleveringa *et al.* 1998) for material (iii) by considering particles ranging over a factor of four in size. Three of these computations, for $h/L = 0.5$, 1 and 2, were taken here to study the effect of size on unloading. The overall stress-strain curves shown in figure 12 show that the hardening rate increases with decreasing size. The continuum model, obviously, does not yield a size effect; the difference seen here is entirely due to the difference in dislocation density and distribution. From these and other simulations, Cleveringa *et al.* (1998) inferred the scaling relation $\mathrm{d}\bar{\tau}/\mathrm{d}\Gamma \propto (h/L)^{-1/3}$. On the other hand, figure 12 shows that the tendency for reverse plasticity during unloading (from $\Gamma \approx 1\%$) is

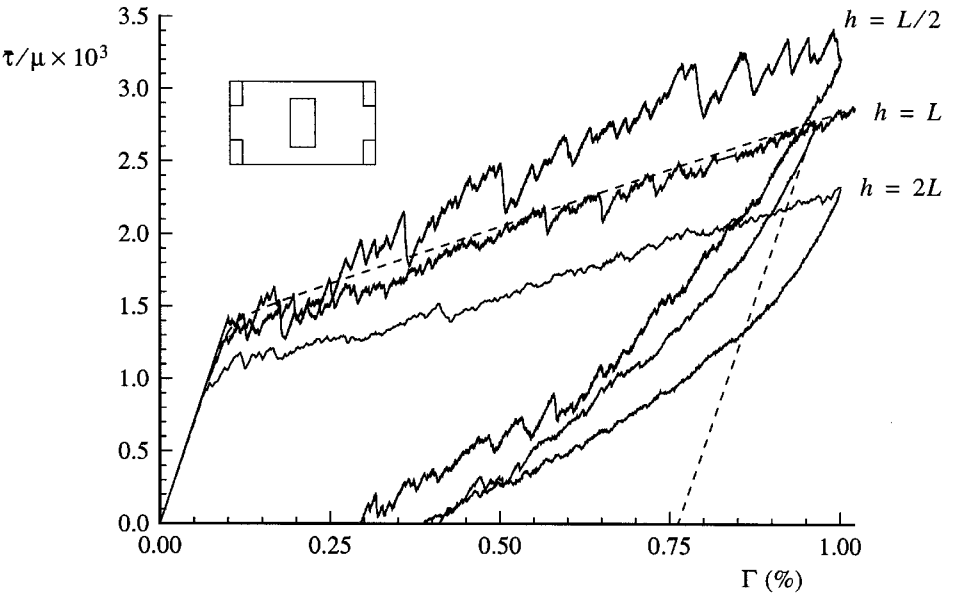

Figure 12. Effect of particle size on the stress–strain response during loading and unloading from $\Gamma \approx 1\%$. The continuum description (- - - -) does not show a size effect.

not notably dependent on size. The results may suggest that the reverse plastic strain rate increases a little with increasing particle size, but this could just be a stochastic effect.

Even though the overall plastic strains after complete unloading are the same for the three cases, the local residual stresses differ enormously. This is demonstrated in figure 13 by comparing the residual shear stresses for $h/L = 0.5$ and 2 (the result for $h = L$ is not shown but is qualitatively similar to that shown in figure 10 (*b*) for the same material but unloaded from $\Gamma = 0.58\%$). Even though the dislocation density for the case with $h/L = 0.5$ (figure 13 (*a*)) is larger than that for $h/L = 2$ (figure 13 (*b*)), the individual stress peaks associated with individual dislocations are seen to be more pronounced for the smaller particle size. Figure 13 suggest that for the largest particle size considered here, the individual stress peaks within the matrix are starting to average out.

In order to see whether indeed these results are approaching the continuum limit, figure 14 shows bar charts of matrix stresses over windows of varying size. As a reference, figure 14 (*a*) pertains to the matrix stresses in the loaded state just before unloading. Figure 14 (*b*) shows the average residual shear stresses, similar to those shown in figure 11. The width of the distributions gradually decreases with increasing size and in fact seems to approach the width of the residual stress distribution according to the continuum plasticity model. The matrix average, however, does not monotonically approach the continuum value. It is likely that, even at the largest size of $h = 2L$, this is due to the organized structure of the dislocations. These results are consistent with the average residual strains $\langle \varepsilon_{[11]} \rangle$ and their standard deviation $[\Psi(\varepsilon_{[11]})]^{1/2}$ computed similarly to the data in tables 2 and 3; the values $\langle \varepsilon_{[11]} \rangle = -266 \times 10^{-6}$ and -250×10^{-6} for $h/L = 0.5$ and 2 respectively differ only slightly from $\langle \varepsilon_{[11]} \rangle = -294 \times 10^{-6}$ for $h = L$ (see table 2), while the standard

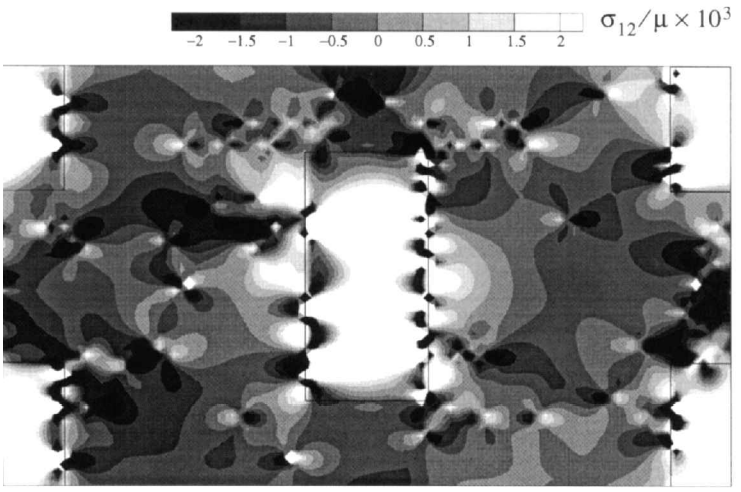

(a)

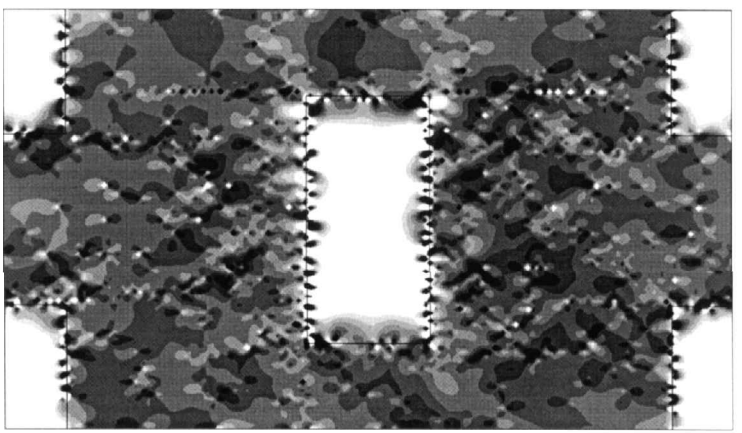

(b)

Figure 13. Residual shear stress distributions after unloading from $\Gamma \approx 1\%$ for materials with (*a*) $h = L/2$ and (*b*) $h = 2L$. Note that the cells are scaled to the same apparent size.

deviation decreases as $[\Psi(\varepsilon_{[11]})]^{1/2} = 0.931 \times 10^{-3}$, 0.877×10^{-3} and 0.708×10^{-3} for $h/L = 0.5$, 1 and 2 respectively.

§4. Discussion

Dispersion-hardened materials with small particles display a large Bauschinger effect and a strong tendency for plastic relaxation in the matrix (for example Clyne and Withers (1993) and P. J. Withers (1997, private communication)). The discrete dislocation simulations of the model composite considered here display these features, and in a very pronounced manner.

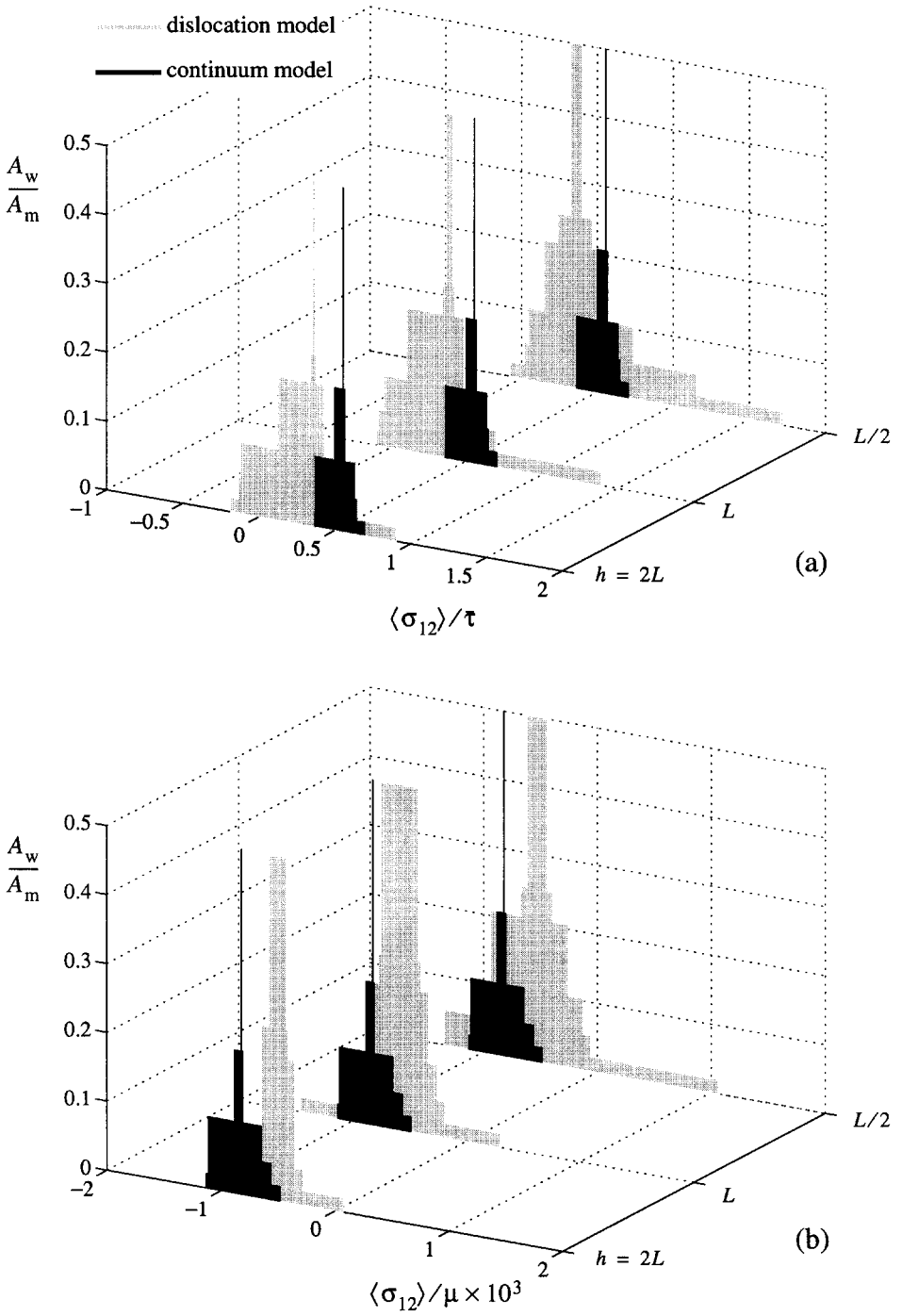

Figure 14. Bar charts of window-averaged residual shear stresses in the matrix of material for three different sizes: $h = L/2$, L and $2L$: (*a*) at $\Gamma \approx 1\%$ during loading (normalized by the current-averaged shear stress $\bar{\tau}$); (*b*) after unloading (cf. figure 13).

Three particle morphologies were analysed. For material (i) there is a vein of unreinforced matrix material, while for materials (ii) and (iii) the reinforcements block every slip plane. When unloading is carried out at the same rate as loading, the amount of reverse plasticity is less for material (i) than for materials (ii) and (iii) (figure 2). Furthermore, the evolution of the dislocation structure during unloading is quite different for materials (ii) and (iii) from that for material (i) (figure 3).

The strong tendency for reverse plasticity found in our simulations can be understood as follows. Dislocation generation and motion during loading of the composite tend to relax the overall stresses in the matrix. The extent of relaxation depends, however, on the rates of these processes in comparison with the applied loading rate. Apparently, complete relaxation does not occur during loading at the loading rates prescribed in our simulations. Thus, there is a driving force for subsequent relaxation by dislocation processes when the composite is unloaded, which gives rise to the large inverse plastic strains during unloading observed in figure 2. High-rate unloading leaves insufficient time for the relaxation to be active (figure 7), but the high driving force remains, and relaxation occurs subsequently once unloading is complete and the material is left in a globally stress-free state (figure 8).

Qualitatively, this is consistent with the behaviour of real particle-hardened materials, but the amount of reverse plasticity, particularly for materials (ii) and (iii), is unrealistically large. There are several reasons for this. First, we have used a unit cell model so that the entire composite has the behaviour of the unit cell in figure 1. Hence, for materials (ii) and (iii) every slip plane in the composite is blocked by a reinforcing particle. Additionally, the density of point obstacles in the matrix was kept constant in our simulations, whereas in real materials the density of forest dislocations and other pinning points for the dislocations on the primary slip planes increase during loading. Thus, in our simulations, relaxation by dislocation motion during unloading is probably unrealistically easy. Allowing for multiple slip in the simulations would most likely give a more realistic unloading behaviour. One should also be aware that the two-dimensional nature of these simulations excludes a number of features of real particle strengthening. In particular, a two-dimensional model cannot allow for the Orowan mechanism where a dislocation line wraps around a particle and leaves an Orowan loop around it once the dislocation has passed.

Plastic flow in the matrix of a composite material, in general, leaves the inclusion in residual tension and the matrix in compression. Here, both the discrete dislocation and the continuum plasticity model give residual matrix shear stresses (figure 11) that are consistent with that. For material (i) the matrix residual shear stress is larger in magnitude than the corresponding value predicted by the continuum plasticity model whereas for materials (ii) and (iii) the reverse is true (table 1). For materials (ii) and (iii), this implies that the average residual stress $\langle\sigma_{12}\rangle^*$ in the particles according to the dislocation model is also smaller than that obtained from the continuum plasticity calculation. This follows immediately from phase equilibrium (9) in the stress-free state, $\bar{\tau} = 0$. This is opposite to what occurs in the loaded state, where a higher proportion of the stress is carried by the particle than is predicted by the continuum slip theory (Cleveringa *et al.* 1997). However, the discrete dislocation description predicts residual stress concentrations locally inside the particles that are very much higher than the maximum stresses according to the continuum theory.

Dislocation considerations of metal matrix composites have often adopted the notion of geometrically necessary dislocations (Ashby 1970). As discussed previously

by Cleveringa *et al.* (1997), the simulation for model material (i) does not lead to geometrically necessary dislocations, while those for materials (ii) and (iii) involve the generation of such dislocations in order to accommodate the rotation of the central particle. This is caused by the fact that in the latter two cases, the particles block every slip plane. The presence of geometrically necessary dislocations explains why material (iii) displays a distinct size effect (see figure 12) while material (i) is essentially size independent. According to Ashby (1970), the density ρ^{G} of geometrically necessary dislocations in the deformed state at an applied strain Γ can be estimated from

$$\frac{\rho^{G}}{\rho} = \frac{2\Gamma}{\rho L^2}\frac{L}{b}\frac{L}{\lambda^{G}}, \tag{11}$$

where λ^{G} is the spacing between particles: $\lambda^{G} = 2(w - w_f) = 2\sqrt{3}(1 - w_f/w)h$. Cleveringa *et al.* (1997) proposed actually to count geometrically necessary dislocations in their simulated dislocation distributions by identifying the net number of dislocations with the same sign at either side of the central particle within a distance of 0.1 times the particle spacing. According to this working definition, the density ratios of geometrically necessary dislocations at $\Gamma \approx 1\%$ for the three sizes presented in figure 12 are $\rho^{G}/\rho \approx 0.46$, 0.32 and 0.28 for $h/L = 0.5$, 1 and 2 respectively. In confronting these results with equation (11), one must account for the fact that the total dislocation density ρ is also size dependent; Cleveringa *et al.* (1998) concluded that ρ scales roughly as $\rho L^2 \propto (h/L)^{-1/3}$ in the simulations for morphology (iii). Thus, equation (11) suggests that $\rho^{G}/\rho \propto (h/L)^{-2/3}$ giving ratios $\rho^{G}/\rho = 1.6 : 1 : 0.6$ for $h/L = 0.5 : 1 : 2$. The ratio of counted densities mentioned above reads $\rho^{G}/\rho = 1.4 : 1 : 0.9$. The value of ρ^{G}/ρ for $h/L = 2$ is 50% larger than expected. Careful consideration of the dislocation distribution (Cleveringa *et al.* 1998) reveals that the stochastic generation of dislocations has led to a larger number of dislocations near the particle interface than geometrically necessary; the associated rotation is counteracted by a clustering of dislocations with opposite Burgers vector at some distance away from the interface.

For materials (ii) and (iii), after unloading to a macroscopically stress-free state, geometrically necessary dislocations are still needed to compensate for the particle rotation associated with the residual shear strain (figure 12). The rotations of the central particle in material (iii) after unloading are 0.24×10^{-2} rad $(h = L/2)$, 0.35×10^{-2} rad $(h = L)$ and are close to the rotations corresponding to the residual shear strains $\Gamma_p = 0.29\%$, 0.41% and 0.39% respectively. According to the estimate (11), the associated density of residual geometrically necessary dislocations satisfies the scaling relation $\rho^{G} L^2/\Gamma_p \propto (h/L)^{-1}$. Using the same working definition for geometrically necessary dislocations as before, actual counting leads to ratios $\rho^{G} L^2/\Gamma_p = 1.63 : 1 : 0.49$ for $h/L = 0.5 : 1 : 2$. For the larger particle size this agrees well; for the smallest size the number of residual dislocations in the cell is too small to identify them reliably to be either geometrically necessary or statistically stored. Residual particle rotations are also predicted by the continuum plasticity model for material (iii), but obviously without a size effect; prior to unloading from $\Gamma = 0.96\%$ the central particles had rotated over 1.1×10^{-2} rad while the rotation reduced to 0.94×10^{-2} rad after unloading $(\Gamma_p = 0.76\%)$. For material (i), there are no dislocations along the particle sides in the unloaded state (figure 4) and there is no residual rotation of the central particle.

A first step towards linking up simulations of this type to diffraction experiments has been made by computing average 'lattice' strains over the matrix and their variance in the unloaded state. The average lattice strains correlate with the position of the peaks in a diffraction profile and the variance contributes to the peak broadening. For material (i), where localization occurs in the discrete dislocation simulation but not in the continuum slip calculation, the discrete dislocation residual lattice shear strain is much larger than the corresponding continuum slip values (table 2). On the other hand, for materials (ii) and (iii) the residual lattice shear strains obtained from the two formulations are comparable, with the values predicted by the continuum slip theory being somewhat larger. Both formulations give rise to lattice normal strains that are much smaller than the lattice shear strain. However, in all cases the discrete dislocation simulations give a much larger variance in the residual lattice shear strain than do the corresponding continuum slip calculations. This is to be attributed to the fluctuations in the strain field that are present in a discrete dislocation representation. Bearing in mind that the actual values of the strain variance calculated from the discrete dislocation results are sensitive to the core cutoff chosen, it is still clear that conventional continuum slip plasticity significantly underestimates the contribution of the strain inhomogeneity in metal matrix composites to the diffraction profile breadth.

ACKNOWLEDGEMENTS

The work of H. H. M. Cleveringa is part of the research programme of the Stichting voor Fundamenteel Onderzoek der Materie which is supported financially by the Nederlandse Organisatie voor Wetenschappelijk Onderzoek. A. Needleman acknowledges support from the Materials Research Science and Engineering Center project 'On Micro- and Nano-Mechanics of Materials' at Brown University (National Science Foundation grant DMR-9632524). We are grateful to Dr P. J. Withers for sharing some unpublished data with us.

APPENDIX A

This appendix outlines the procedure to perform the discrete dislocation, recovery computations discussed in § 3.1 under overall shear stress-free conditions. This special procedure is necessary since we impose kinematic boundary conditions in equation (1) and need to determine Γ in order that $\bar{\tau} = 0$ (cf. equation (2)).

Given the distribution of dislocations at some instant, all fields denoted by a tilde are known and the fields denoted by a hat are governed by the equations

$$\nabla \cdot \hat{\boldsymbol{\sigma}} = 0, \quad \hat{\boldsymbol{\varepsilon}} = \mathrm{sym}(\nabla \otimes \hat{\mathbf{u}}), \tag{A 1}$$

and

$$\begin{aligned} \hat{\boldsymbol{\sigma}} &= \boldsymbol{\mathcal{L}} : \hat{\boldsymbol{\varepsilon}} && \text{in the matrix,} \\ \hat{\boldsymbol{\sigma}} &= \boldsymbol{\mathcal{L}}^* : \hat{\boldsymbol{\varepsilon}} + \tilde{\mathbf{p}} && \text{in the reinforcement} \end{aligned} \tag{A 2}$$

($\boldsymbol{\mathcal{L}}$ and $\boldsymbol{\mathcal{L}}^*$ denoting the elastic modulus tensors of matrix and particles respectively) where the polarization stress tensor $\tilde{\mathbf{p}} = (\boldsymbol{\mathcal{L}}^* - \boldsymbol{\mathcal{L}}) : \tilde{\boldsymbol{\varepsilon}}$ is specified entirely by the fields denoted by a tilde. The associated boundary conditions (cf. equation (1)) are

$$\hat{u}_1(x_1, \pm h) = \pm U - \tilde{u}_1(x_1, \pm h) \quad \hat{u}_2(x_1, \pm h) = -\tilde{u}_2(x_1, \pm h). \tag{A 3}$$

The condition that the overall shear stress (cf. equation (2)) vanishes leads to the following constraint upon the $\hat{\sigma}_{12}$ field along the boundaries:

$$\int_{-w}^{w} \hat{\sigma}_{12}(x_1, \pm h)\, \mathrm{d}x_1 = -\int_{-w}^{w} \tilde{\sigma}_{12}(x_1, \pm h)\, \mathrm{d}x_1, \tag{A 4}$$

The value of U that satisfies all equations (A 1)–(A 4) is found by writing the field denoted by a circumflex as a superposition of two solutions.

(1) The fields $\{\hat{\mathbf{u}}^{(1)}, \hat{\boldsymbol{\varepsilon}}^{(1)}, \hat{\boldsymbol{\sigma}}^{(1)}\}$ are the solution to the set of equations (A 1) and

$$\hat{\boldsymbol{\sigma}}^{(1)} = \boldsymbol{\mathcal{L}} : \hat{\boldsymbol{\varepsilon}}^{(1)} \quad \text{in the matrix,}$$

$$\hat{\boldsymbol{\sigma}}^{(1)} = \boldsymbol{\mathcal{L}}^* : \hat{\boldsymbol{\varepsilon}}^{(1)} + \tilde{\mathbf{p}} \quad \text{in the reinforcement,} \tag{A 2}$$

under the boundary conditions

$$\hat{u}_1^{(1)}(x_1, \pm h) = -\tilde{u}_1(x_1, \pm h) \quad \hat{u}_2^{(1)}(x_1, \pm h) = -\tilde{u}_2(x_1, \pm h), \tag{A 5}$$

specifying zero applied strain.

(2) The fields $\{\hat{\mathbf{u}}^{(2)}, \hat{\boldsymbol{\varepsilon}}^{(2)}, \hat{\boldsymbol{\sigma}}^{(2)}\}$ are the solution to the set of equations (A 1) and

$$\hat{\boldsymbol{\sigma}}^{(2)} = \boldsymbol{\mathcal{L}} : \hat{\boldsymbol{\varepsilon}}^{(2)} \quad \text{in the matrix,}$$

$$\hat{\boldsymbol{\sigma}}^{(2)} = \boldsymbol{\mathcal{L}}^* : \hat{\boldsymbol{\varepsilon}}^{(2)} + \tilde{\mathbf{p}} \quad \text{in the reinforcement,} \tag{A 6}$$

under the boundary conditions

$$\hat{u}_1^{(2)}(x)_1, \pm h) = \pm U_0 \quad \hat{u}_2^{(2)}(t) = 0. \tag{A 6}$$

specifying zero applied strain. Thus, the second solution considers only the applied loading and ignores the dislocation fields. The prescribed displacement U_0 is an arbitrary trial displacement.

The solution

$$\hat{\mathbf{u}} = \hat{\mathbf{u}}^{(1)} + \lambda \hat{\mathbf{u}}^{(2)}, \quad \hat{\boldsymbol{\varepsilon}} = \hat{\boldsymbol{\varepsilon}}^{(1)} + \lambda \hat{\boldsymbol{\varepsilon}}^{(2)}, \quad \hat{\boldsymbol{\sigma}} = \hat{\boldsymbol{\sigma}}^{(1)} + \lambda \hat{\boldsymbol{\sigma}}^{(2)},$$

with $U = \lambda U_0$, satisfies the governing equations (A 1)–(A 3). The scaling factor λ is determined so that the condition (A 4) is satisfied, that is

$$\lambda = -\frac{\int_{-w}^{w} \tilde{\sigma}_{12}(x_1, \pm h)\, \mathrm{d}x_1 + \int_{-w}^{w} \hat{\sigma}_{12}^{(1)}(x_1, \pm h)\, \mathrm{d}x_1}{\int_{-w}^{w} \hat{\sigma}_{12}^{(2)}(x_1, \pm h)\, \mathrm{d}x_1}. \tag{A 7}$$

In this paper, the above equations are dealt with in their usual finite-element discretized form. The scaling factor λ is calculated separately for $x_2 = h$ and $x_2 = -h$. Because of numerical errors, these respective values need not be identical, but they were found to be the same to within four significant digits for all cases presented.

References

Allen, A. J., Bourke, M., Dawes, S., Hutchings, M. T., and Withers, P. J., 1992, *Acta metall. mater.,* **40**, 2361.

Arsenault, R. J., and Taya, M., 1987, *Acta metall. mater.,* **35**, 651.

Asaro, R. J., 1983, *Adv. appl. Mech.,* **23**, 1.

Ashby, M. F., 1970, *Phil. Mag.,* **21**, 399.

Bassani, J. L., 1994, *Adv. appl. Mech.,* **30**, 191.

Cleveringa, H. H. M., Van der Giessen, E., and Needleman, A., 1997, *Acta mater.,* **45**, 3163; 1998, *J. de Phys.* IV, **8**, 83.

Clyne, T. W., Withers, P. J., 1993, *An Introduction to Metal Matrix Composites* (Cambridge University Press).

Cuitiño, A. M., and Ortiz, M., 1992, *Modelling Simulation Mater. Sci. Engng,* **1**, 225.

Fivel, M. C., Gosling, T. J., and Canova, G. R., 1996, *Modelling Simulation Mater. Sci. Engng.,* **4**, 581.

Hirth, J. P., and Lothe, J., 1968, *Theory of Dislocations* (New York: McGraw-Hill).

Krawitz, A. D., Crapenhoft, M. L., Reichel, D. G., and Warren, R., 1988, *Mater. Sci. Engng.,* **A105–106**, 275.

Kubin, L. P., Canova, G., Condat, M., Devincre, B., Pontikis, V., and Bréchet, Y., 1992, *Nonlinear Phenomena in Materials Science II,* edited by G. Martin and L. P. Kubin (Vaduz: Sci-Tech), p. 455.

Levy, A., and Papazian, J. M., 1991, *Acta metall. mater.,* **39**, 2255.

Lubarda, V., Blume, J. A., and Needleman, A., 1993, *Acta metall. mater.,* **41**, 625.

Nabarro, F. R. N., 1967, *Theory of Crystal Dislocations* (Oxford University Press).

Nan, C.-W., and Clarke, D. R., 1996, *Acta mater.,* **44**, 3801.

Noyan, I. C., and Cohen, J. B., 1987, *Residual Stress—Measurement by Diffraction and Interpretation* (Berlin: Springer).

Peirce, D., Asaro, R. J., and Needleman, A., 1983, *Acta metall.,* **31**, 1951.

Polonsky, I. A., and Keer, L. M., 1996, *Proc. R. Soc. Lond.* A, **452**, 2173.

Povirk, G. L., Stout, M. G., Bourke, M., Goldstone, J. A., Lawson, A. C., Lovato, M., MacEwen, S. R., Nutt, S. R., and Needleman, A., 1992, *Acta metall. mater.,* **40**, 2391.

Stokes, A. R., and Wilson, A. J. C., 1944, *Proc. phys. Soc.,* **56**, 174.

Taggert, D. G., and Bassani, J. L., 1991, *Mech. Mater.,* **12**, 63.

Tsai, S.-D., Mahulikar, D., Markus, H. L., Noyan, I. C., and Cohen, J. B., 1981, *Mater. Sci. Engng,* **47**, 145.

Tvergaard, V., 1991, *Mech. mater.,* **11**, 149.

Van der Giessen, E., and Needleman, A., 1995, *Modelling Simulation Mater. Sci. Engng.,* **3**, 689.

Warner, T. J., and Stobbs, W. M., 1989, *Acta metall.,* **37**, 2873.

Warren, B. E., 1969, *X-ray Diffraction* (Reading: Massachusetts: Addison-Wesley).

Weisbrook, C. M., and Krawitz, A. D., 1996. *Mater. Sci. Engng.,* **A209**, 318.

Withers, P. J., Stobbs, W. M., and Pederson, O. B., 1989, *Acta metall.,* **37**, 3061.

Zacharopoulos, N., Srolovitz, D. J., and LeSar, R., 1997, *Acta mater.,* **45**, 3745.

Zahl, D. B., and McMeeking, R. M., 1991, *Acta metall. mater.*, **39**, 1117.

Zywicz, E., and Parks, D. M., 1988, *Comput. Sci. Technol.,* **33**, 295.